

An Iterative Ensemble Square Root Filter and Tests with Simulated Radar Data for Storm Scale Data Assimilation

Shizhang Wang^{1,2}, Ming Xue^{2,3*}, Alexander D. Schenkman^{2,3}, and Jinzhong Min¹

¹Jiangsu Key Laboratory of Meteorological Disaster
Nanjing University of Information Science and Technology¹
Nanjing 210044, China

²Center for Analysis and Prediction of Storms and ³School of Meteorology
University of Oklahoma, Norman Oklahoma 73072

January 2012

Submitted to Quarterly Journal of Royal Meteorological Society

*Corresponding author address:
Ming Xue
Center for Analysis and Prediction of Storms
University of Oklahoma,
120 David L. Boren Blvd, Norman OK 73072
mxue@ou.edu

Abstract

An iterative procedure is designed to accelerate the ‘spin-up’ of ensemble square root filter (EnSRF) data assimilation cycles when starting from a poor initial ensemble. Referred to as “iterative EnSRF” (iEnSRF), this procedure follows the “running in place” (RIP) concept developed for the local ensemble transform Kalman filter (LETKF) but is implemented differently due to algorithm differences. iEnSRF is a three step procedure: First, a backward EnSRF analysis is performed that updates the ensemble model states at an earlier time. Second, an ensemble of forecasts is run from these updated model states to the analysis time. These two steps are then repeated a pre-specified number of times. The backward analysis is performed via asynchronous Ensemble Kalman filter (EnKF) which is capable of assimilating observations collected at times different than the analysis time. Like RIP, iEnSRF uses the same observations repeatedly during the initial assimilation cycles, allowing for the extraction of additional information from observations when estimated ensemble mean state and ensemble covariance are poor.

The iEnSRF algorithm is tested using simulated radar data for an idealized supercell storm. In experiments with a perfect model and correct storm environment, as well as in the presence of model and environmental errors, iEnSRF reduces the analysis error in the first few cycles more quickly than the regular EnSRF, leading to improved subsequent short-range forecasts. After the first few analysis cycles, continued use of iterations does not lead to further improvement. The better performance of iEnSRF appears to be the result of improved background error covariance estimation as well as improved state estimation in the first few cycles, especially for correlations between observed and unobserved variables. Through iterations, iEnSRF is also able to reach a steady level of state estimation error in a more quickly than the corresponding non-iterated version.

Keywords: Radar Data Assimilation, Iterative Procedure, Ensemble Kalman Filter.

1. Introduction

The ability of ensemble Kalman filter (EnKF) (Evensen 1994, 2003) to initialize convective storms from simulated Doppler radar radial velocity data was first demonstrated by (Snyder and Zhang 2003) and (Zhang et al. 2004) within an anelastic cloud model with simplified warm rain microphysics. Subsequent studies by (Tong and Xue 2005) and (Xue et al. 2006) demonstrated the capability of EnKF to assimilate radar radial velocity as well as reflectivity data into a compressible model with complex ice microphysics. More recent studies have found that the ability to handle complex nonlinear physics important for convective storms is an advantage the EnKF method has over other data assimilation procedures (Jung et al. 2008; Xue et al. 2010; Snook et al. 2011).

The EnKF is based on Monte Carlo sampling in which an ensemble is used to sample the model state uncertainty and to evolve the model state error covariance (Evensen 1994). An optimal analysis can be only be obtained if two independent requirements are satisfied: (i) the ensemble mean is close enough to the truth and (ii) the ensemble perturbations are representative of the true error characteristics (Kalnay and Yang 2010).

For convective storms, Doppler weather radar is generally the only observation platform capable of providing detailed observations of the wind and precipitation structures within the storms. Due to sensitivity limitations, Doppler radar data are usually only available after precipitation-sized particles form, posing a challenge for the initialization of rapidly developing storms, especially for cycled data assimilation (DA) methods that require the assimilation of many volume scans of radar data before a reasonably accurate estimate of the state of atmosphere can be obtained.

EnKF DA cycles for convective storms typically start from a first guess field that only contains information about the broader-scale storm environment. Observing system simulation experiment (OSSE) studies have shown that it typically takes more than 10 assimilation cycles to obtain accurate analyses of convective storms when assimilating Doppler radar data via EnKF (Caya et al. 2005; Xue et al. 2006; Yussouf and Stensrud 2010). (Caya et al. 2005) showed that because of the iterative nature of a four dimensional variational (4DVAR) method, 4DVAR is able to establish a reasonably accurate analysis of a convective storm by assimilating only 1-2 radar volume scans. EnKF takes substantially longer to achieve this level accuracy, but is able to produce a more accurate analysis than 4DVAR after several additional assimilation cycles. With the standard precipitation-mode volume scan interval of about 5 minutes for the operational WSR-88D weather radars of the U.S., (Xue et al. 2006) showed that it took about 50 minutes for EnKF to establish a well-defined storm, which is confirmed by (Yussouf and Stensrud 2010). However, given a rapidly developing severe storm, as noted in (Kalnay and Yang 2010), such a spin-up time is likely to result in the EnKF analysis being less useful for severe storm forecast than 4DVAR (Caya et al. 2005).

The desire to accelerate the ‘convergence’ (i.e., reduce the ‘spin up time’) of EnKF DA cycles, so that reasonably accurate state and covariance estimations can be established more rapidly, motivated the development of an iterative procedure called ‘running-in-place (RIP)’ by (Kalnay and Yang 2010), in a local ensemble transform Kalman filter (LETKF) (Hunt et al. 2007) framework. RIP is a three-step procedure: (i) a “no-cost” ensemble Kalman smoother (EnKS) (Kalnay et al. 2007; Yang et al. 2009) is used to go backward in time within an assimilation cycle to improve the background state at the pre-

vious time, (ii) advance with the standard LETKF procedure from the updated background and (iii) repeat steps (i) and (ii) until a desired state is reached. Because it is based on the LETKF algorithm, the ‘no-cost’ EnKS uses LETKF weights obtained with observations at the later time to update ensemble states at the earlier time, hence improving both the state and covariance at the earlier time and allowing for the repetitive use of the observations within an assimilation cycle. (Kalnay and Yang 2010) found that within an idealized global primitive equation model the RIP procedure improve the quality of the initial ensemble mean and background error covariance, so that fewer cycles are required for the filter to approach its optimal analysis. This result is especially true when initial ensemble perturbations are Gaussian noise and/or when the initial ensemble mean is far from the truth. The latter situation is often realized in thunderstorm initialization.

Although the RIP procedure was originally motivated by issues observed in storm-scale data assimilation, such a procedure has never been applied to the storm-scale DA problem. Testing such an idea in storm-scale DA is the main purpose of this paper. Almost all storm-scale radar DA studies to date have used either the ensemble square root filter (EnSRF) (Whitaker and Hamill 2002) algorithm or the original EnKF algorithm with perturbed observations (Tong and Xue 2005). Such algorithms are serial and process observations one at a time. To apply the RIP idea to the EnSRF algorithm, we have developed a new procedure called iterative EnSRF (iEnSRF).

As an initial evaluation of iEnSRF, we perform a set of OSSEs with simulated radar observations for a supercell storm. The OSSEs are conducted first for a perfect model experiment with no storm environment error and then in the presence of prediction model and storm environment errors. Environment error is generated by adding perturbations to

the environmental sounding and model error is simulated by using different physical parameterization schemes in the ensemble forecasts. The benefits of iEnSRF as compared to the regular EnSRF are assessed for these different situations.

The remainder of this paper is organized as follows. In section 2, the iEnSRF algorithm is described and contrasted with RIP. Section 3 provides the configurations of the prediction model and data assimilation, and describes the simulation of radar observations and the design of OSSEs. The results of the OSSEs are discussed in section 4 and a summary is given in section 5.

2. The EnSRF and iEnSRF algorithms

2.1. The EnSRF algorithm

We first give a brief summary of the standard EnSRF algorithm on which iEnSRF is based. Following (Whitaker and Hamill 2002), the serial EnSRF algorithm analyzes uncorrelated observations one after another. Therefore, the observation error covariance \mathbf{R} and background error covariance mapped to the observation space, $\mathbf{HP}^b\mathbf{H}^T$, reduce to scalars. The analysis equations for updating the ensemble mean model state $\bar{\mathbf{x}}$ and the i^{th} ensemble deviation from the mean, \mathbf{x}'_i , are,

$$\bar{\mathbf{x}}^a = \bar{\mathbf{x}}^b + \mathbf{K}(y_j^o - \overline{H(\mathbf{x}^b)}), \quad (1)$$

$$\mathbf{x}_i^a = \mathbf{x}_i^b + \alpha \mathbf{K}[H(\mathbf{x}_i^b) - \overline{H(\mathbf{x}^b)}], \quad (2)$$

where

$$\mathbf{K} = \mathbf{P}^b\mathbf{H}^T (\mathbf{HP}^b\mathbf{H}^T + \mathbf{R})^{-1}, \quad (3)$$

is the Kalman gain matrix, \mathbf{P}^b is the background error covariance, H is the observation operator mapping variables from model state space to observation space, and \mathbf{H} is a linearized version of H . Here, superscripts a, b, and o denote the analysis, background and observation, respectively. Subscripts i and j denote the i^{th} ensemble member and the j^{th} observation, respectively. In Eq. (2),

$$\alpha = [1 + \sqrt{\mathbf{R}(\mathbf{H}\mathbf{P}^b\mathbf{H}^T + \mathbf{R})^{-1}}]^{-1} \quad (4)$$

is a coefficient derived by (Whitaker and Hamill 2002) for the EnSRF algorithm. Equation (4) is only valid for single observation analysis and therefore both the numerator and denominator inside the square root are scalars. The background error covariance terms in \mathbf{K} are estimated using the ensemble members, according to

$$\mathbf{P}^b\mathbf{H}^T = \frac{1}{N-1} \sum_{i=1}^N (\mathbf{x}_i^b - \bar{\mathbf{x}}^b) [H(\mathbf{x}_i^b) - \overline{H(\mathbf{x}^b)}]^T, \quad (5)$$

$$\mathbf{H}\mathbf{P}^b\mathbf{H}^T = \frac{1}{N-1} \sum_{i=1}^N [H(\mathbf{x}_i^b) - \overline{H(\mathbf{x}^b)}][H(\mathbf{x}_i^b) - \overline{H(\mathbf{x}^b)}]^T, \quad (6)$$

where N is the ensemble size. For each observation, $\mathbf{P}^b\mathbf{H}^T$ is a vector and $\mathbf{H}\mathbf{P}^b\mathbf{H}^T$ is a scalar. Observations are analyzed by using Eq. (1) and Eq. (2) sequentially, one after another. After all observations at a given time are analyzed, an ensemble of forecasts proceeds from the analysis ensemble until new observations are available; the analysis cycles are then repeated.

2.2. The *iEnSRF* algorithm

As mentioned earlier, our iterative EnSRF procedure follows the RIP concept and also involves three steps in each analysis cycle, but its implementation differs from that of RIP due to differences between the LETKF and EnSRF algorithms on which they are

based. This is particularly true for the first step where an earlier state is updated using later observations. This subsection describes the details of iEnSRF while pointing out its differences with RIP.

In LETKF, the final ensemble analyses are obtained as linear combinations of the background ensemble forecasts, using transformation weights determined by the LETKF algorithm (Hunt et al. 2007). In the first step of RIP (Kalnay and Yang 2010), the “weights” obtained at the current time, t_n , are used to transform the ensemble forecasts at a previous time, t_{n-1} , into updated states or ensemble analyses valid at t_{n-1} . This procedure is referred to as ‘no-cost’ EnKS (Kalnay et al. 2007; Yang et al. 2009). EnSRF has no such weights, at least not explicitly, thus requiring a different procedure to update the previous time.

Specifically, in EnSRF, an asynchronous implementation can be done so that observations at the current time can be used to update states at an earlier time. An algorithm to implement such asynchronicity was developed by (Sakov et al. 2010) and can be applied to different variants of EnKF. However, due to the serial nature of EnSRF, the implementation of the asynchronous algorithm has additional complications. In a typical asynchronous algorithm, observation priors computed at t_n , the time of observations, are used to update the model state at t_{n-1} . This usually requires the pre-calculation and simultaneous use of all observation priors, as described in (Sakov et al. 2010); this is not possible for the serial EnSRF.

To address this complication, we treat the state vector \mathbf{x} at t_{n-1} as an extension of the state vector at t_n and form an extended state vector $(\mathbf{x}_{t_n}^T, \mathbf{x}_{t_{n-1}}^T)^T$. This extended state vector is treated like a regular vector in EnSRF, and both state vectors are updated by the

filter simultaneously. It is then straightforward to apply the asynchronous algorithm. This is similar to the joint state-observation vector used by (Anderson 2001). Through this new vector, the update of observation priors at t_n follows the standard EnSRF algorithm and it is possible to analyze the model state at t_{n-1} from observations available at t_n . Here, the update of state at t_{n-1} by data available at t_n is achieved through asynchronous covariance which involves model state samples distributed in time. The asynchronous covariance for updating model state at t_{n-1} using observations t_n are

$$\mathbf{P}_{t_{n-1}}^b \mathbf{H}^T = \frac{1}{N-1} \sum_{i=1}^N (\mathbf{x}_{i,t_{n-1}}^b - \bar{\mathbf{x}}_{t_{n-1}}^b) [H(\mathbf{x}_{i,t_n}^b) - \overline{H(\mathbf{x}_{t_n}^b)}]^T, \quad (7)$$

$$\mathbf{HP}_{t_n}^b \mathbf{H}^T = \frac{1}{N-1} \sum_{i=1}^N [H(\mathbf{x}_{i,t_n}^b) - \overline{H(\mathbf{x}_{t_n}^b)}] [H(\mathbf{x}_{i,t_n}^b) - \overline{H(\mathbf{x}_{t_n}^b)}]^T, \quad (8)$$

where $\mathbf{P}_{t_{n-1}}^b \mathbf{H}^T$ is the covariance between model states at t_{n-1} and observation priors at t_n , $\mathbf{HP}_{t_n}^b \mathbf{H}^T$ is the same as that in Eq. (6) because the observations used to update $\mathbf{x}_{t_{n-1}}$ are valid at t_n . Therefore, the Kalman gain matrix $\mathbf{K}_{t_{n-1}}$ for updating model state $\mathbf{x}_{t_{n-1}}$ is calculated according to

$$\mathbf{K}_{t_{n-1}} = \mathbf{P}_{t_{n-1}}^b \mathbf{H}^T (\mathbf{HP}_{t_n}^b \mathbf{H}^T + \mathbf{R})^{-1}. \quad (9)$$

Then, the analysis equations for ensemble mean ($\bar{\mathbf{x}}_{t_{n-1}}$) and ensemble deviations ($\mathbf{x}'_{i,t_{n-1}}$) are, respectively,

$$\bar{\mathbf{x}}_{t_{n-1}}^a = \bar{\mathbf{x}}_{t_{n-1}}^b + \mathbf{K}_{t_{n-1}} (y_j^o - \overline{H(\mathbf{x}_{t_n}^b)}), \quad (10)$$

$$\mathbf{x}'_{i,t_{n-1}}^a = \mathbf{x}'_{i,t_{n-1}}^b + \alpha \mathbf{K}_{t_{n-1}} (H(\mathbf{x}_{i,t_n}^b) - \overline{H(\mathbf{x}_{t_n}^b)}). \quad (11)$$

Through Eqs. (10) and (11), the model states at t_{n-1} can be updated by observations taken at t_n . Because Eqs. (10) and (11) are similar to Eqs. (1) and (2), except for the Kalman

gain, it is easy to implement within an existing EnSRF framework. Once the ensemble states at t_{n-1} are updated, ensemble forecasts from t_{n-1} are produced to arrive at new forecast states at t_n and such new forecast states are used in the next iteration of asynchronous filter updating. The iterations are repeated in a similar manner as in (Kalnay and Yang 2010). Because of the use of an updated state at t_{n-1} , the updated forecast states at t_n should be improved over that of the earlier iteration.

Our iEnSRF procedure is illustrated in Figure 1. It should be pointed out that, as part of an extended state, \mathbf{x}_{i,t_n} and $\mathbf{x}_{i,t_{n-1}}$ must be simultaneously updated (note that in the figure, model states at t_{n-1}^* instead of t_{n-1} are updated, this will be discussed later in this section). It is noted that only the updated \mathbf{x}_{i,t_n} in the final iteration are carried into the next assimilation cycle, while those in the intermediate iterations are only needed for calculating covariance for the next observation. Obviously, this is computationally inefficient. A possible solution to this problem follows the scalable implementation of an ensemble filter proposed by (Anderson and Collins 2007), which pre-calculates and updates observation priors as part of an extended state. By updating the observation priors at t_n instead of the full state, the number of calculations can be greatly reduced; \mathbf{x}_{i,t_n} will then only need to be updated in the final iteration. This approach is only equivalent to state updating when the observation operator is linear. In practice, differences due to such an approximation are likely no larger than other sources of uncertainty within a filter implementation (Anderson and Collins 2007). While this approach is attractive, computational efficiency is not the focus in this proof of concept paper, and we chose to keep the implementation simple based on an existing EnSRF code.

Asynchronous algorithms are subject to temporal sampling error, in addition to spatial sampling error. Similar to the spatial sampling error, temporal sampling error can cause erroneous correlations when the time interval between samples is long. A temporal localization is introduced to help minimize such effects. In this study, the fifth-order correlation function (Gaspari and Cohn 1999), typically used for spatial localization, is employed for temporal localization. Spatial and temporal localization are applied simultaneously to all state variables. With the spatiotemporal localization, analysis equations for updating ensemble mean $\bar{\mathbf{x}}_{t_{n-1}}$ and ensemble deviations $\mathbf{x}'_{i,t_{n-1}}$ are modified from those in (10) and (11),

$$\bar{\mathbf{x}}_{t_{n-1}}^a = \bar{\mathbf{x}}_{t_{n-1}}^b + (\rho_{tl} \boldsymbol{\rho}_{sl}) \circ \mathbf{K}_{t_{n-1}} (y_j^o - \overline{H(\mathbf{x}_{t_n}^b)}), \quad (12)$$

$$\mathbf{x}_{i,t_{n-1}}^{ia} = \mathbf{x}_{i,t_{n-1}}^{ib} + \alpha (\rho_{tl} \boldsymbol{\rho}_{sl}) \circ \mathbf{K}_{t_{n-1}} (H(\mathbf{x}_{i,t_n}^b) - \overline{H(\mathbf{x}_{t_n}^b)}), \quad (13)$$

where scalar ρ_{tl} is the temporal localization coefficient; vector $\boldsymbol{\rho}_{sl}$ contains the spatial localization coefficients and “ \circ ” represents the Schur (elementwise) product (Houtekamer and Mitchell 2001). ρ_{tl} is a scalar that is a function of the time interval between t_{n-1} and t_n while $\boldsymbol{\rho}_{sl}$ is a vector because the distance between y_j^o and model grid points can vary.

Another important consideration in our iterative procedure is how to determine the time interval of iteration between t_{n-1} and t_n . According to (Kalnay and Yang 2010), RIP updates the state at t_{n-1} even though observations are available at t_n . They justified such a procedure on the grounds that the EnKS updated ensemble at t_{n-1} is more accurate than the analysis ensemble using data only at t_{n-1} (Yang et al. 2009; Kalnay and Yang 2010). However, studies have not yet been conducted to confirm that asynchronous

EnKF can generate better analysis at t_{n-1} by using observations valid at t_n instead of t_{n-1} . In other words, if observations are available at t_{n-1} , they are usually used to update the state at t_{n-1} , rather than updating the state at t_{n-1} with observations valid at t_n . To avoid this complication, in our implementation, iterations are carried out between t_n and t_{n-1}^* , where t_{n-1}^* is an intermediate time between t_{n-1} and t_n when no observation is available. The other consideration in using t_{n-1}^* rather than t_n is that the desired the temporal localization can limit the time interval of iteration because the correlation coefficient is reduced to zero outside the cutoff radius of temporal localization; the asynchronous updating should occur within the time localization window. A longer time interval of iteration also costs more computationally because of the longer, repetitive, ensemble forecasts involved; tuning of an iterative procedure will likely need to balance analysis quality and computational cost.

3. The observing system simulation experiments

3.1. The prediction model settings and truth simulation

The non-hydrostatic and fully compressible Weather Research and Forecast (WRF) model V2.2.1 is used to produce the truth simulation of an idealized supercell storm and for the OSSEs. For all experiments, the physical domain used is $60 \text{ km} \times 60 \text{ km} \times 20 \text{ km}$. The model domain has a horizontal grid spacing of 2 km and a vertical grid spacing of 0.5 km. The truth simulation is initialized from the classic (Weisman and Klemp 1982) analytic sounding provided in WRF package (plotted in Fig. 2 along with a modified sounding to be discussed later). The CAPE of the sounding is about 2000 J kg^{-1}

with directional (clockwise) vertical wind shear that favors right-moving cells following storm splitting (Klemp 1987). The storm is triggered by an ellipsoidal thermal bubble centered at $x = 14$, $y = 28$ and $z = 1.5$ km, with a 10-km horizontal radius and a 1.5-km vertical radius and a 3 K maximum temperature perturbation. Other model configurations include: Runge-Kutta 3rd-order time-integration scheme with a time step of 12 seconds, WRF Single-Moment 6-class (WSM6) microphysics parameterization scheme, and the Rapid Radiative Transfer Model (RRTM) and Dudhia schemes for long and short wave radiation. No cumulus parameterization is included. A 1.5-order turbulent kinetic energy (TKE) closure scheme is used to parameterize subgrid-scale turbulence and a positive definite scheme is used for the advection of moisture and water variables. Open conditions are used at the lateral boundaries. More details with regard to schemes in WRF V2 are described in (Skamarock et al. 2005). The length of the truth simulation is 90 minutes.

We now briefly describe the truth simulation. In this paper, all times are relative to the initial time (0 min) of the truth simulation. At 40 min (Figure 3a), two updraft cores are found at mid-levels, resulting from storm splitting. One core is located in the southern part of the rear of storm with the other located to the north. The southern cell (hereafter, SC) is stronger than the northern cell (hereafter, NC). The maximum updraft in SC at this time reaches 25 m s^{-1} at 5 km above ground level (AGL). At 90 min (Figure 3b), SC is located in the southeastern portion of the model domain, about 28 km from the position of initial thermal bubble (shown with a red dot in Figure 3b). The maximum updraft is greater than 30 m s^{-1} at 5 km AGL. Meanwhile, in the northern part of the model domain, the region of graupel associated with NC becomes larger than that with SC even though its updraft is still weaker. Plots at higher altitudes (not shown) feature a larger re-

gion of hydrometeors for SC, indicative of a deeper updraft for SC than NC. Throughout the simulation period, the storm top of SC reaches about 15 km and its maximum updraft reaches 40 m s^{-1} . This classic splitting supercell storm serves as the truth storm from which simulated radar data will be created for OSSEs.

3.2. Simulation of radar observations

A simulated WSR-88D type of radar is placed at $x = -22 \text{ km}$ and $y = 78 \text{ km}$. This location is outside the model domain and about 60 km to the northwest of initial thermal bubble. Following recent OSSE papers of (Xue et al. 2006) and (Zhang and Rosati 2010), the simulated observations are sampled on radar elevations rather than at model grid points (Snyder and Zhang 2003; Tong and Xue 2005). Radar observations are simulated from model variables interpolated to the model scalar points in horizontal direction and radar elevation in vertical direction, as is common practice (Crook et al. 2004). The radar operates in the standard U.S. operational WSR-88D radar precipitation scan mode (VCP 11), with 14 elevation levels and 5 minute volumes scan intervals. Following (Zhang and Rosati 2010), the lower 12 sweeps of observations are generated at a rate of 3 sweeps per minute and the upper 2 sweeps are generated in the final minute of each volume scan. To take into account measurement and sampling error of radial velocity (V_r) and reflectivity observations (Z), random errors of zero mean and standard deviations of 2 m s^{-1} and 2dBZ are added to V_r and Z , respectively. The operator for V_r is

$$V_r = u_g \cos \alpha \sin \beta + v_g \cos \alpha \cos \beta + (w_g - w_t) \sin \alpha, \quad (14)$$

where u_g , v_g and w_g are model-simulated velocities interpolated from the staggered model grid points to the observation location using tri-linear interpolation; w_t is the mean

terminal fall speed of hydrometeors; α and β are the elevation and azimuth angles of the radar beam, respectively. The simulated reflectivity, Z , in dBZ is calculated from the mixing ratios of rainwater, snow, and graupel using the formulations of (Tong and Xue 2005) and (Xue et al. 2006). The operator for Z satisfies the relationship

$$Z = 10 \log_{10} \left(\frac{Z_r + Z_s + Z_h}{1 \text{ mm}^6 \text{ m}^{-3}} \right), \quad (15)$$

where Z_r , Z_s and Z_h are equivalent reflectivity factors for rainwater, snow and graupel, respectively. Observations used in the assimilation experiments are calculated from Eqs. (14) and (15) with added random errors. Radial velocity and reflectivity are only assimilated where reflectivity exceeds 10 dBZ.

3.3. Data assimilation settings

Forty ensemble members are used in all experiments. Similar to (Tong and Xue 2005), ensemble forecasts begin 20 min into the simulation when the storm cell first develops from the thermal bubble. Random perturbations are added to a first guess state to create an ensemble of initial conditions. These random perturbations have a Gaussian distribution with zero mean and standard deviation of 3 K for perturbation potential temperature θ' (defined as total potential temperature θ minus 300 K) and 0.5 g kg^{-1} for water vapor mixing ratio q_v . The wind field is not perturbed. Perturbations are only added at the grid points where reflectivity greater than 10 dBZ is observed within 2 km to avoid spurious convection outside the observed area. After all the observations at an analysis time are analyzed, the relaxation method of inflation (Zhang et al. 2004) is used to overcome insufficient ensemble spread. Following (Zhang et al. 2004), the formula for relaxation inflation is

$$(\mathbf{x}_{new}^a)' = (1 - \gamma)(\mathbf{x}^a)' + \gamma(\mathbf{x}^b)', \quad (16)$$

where γ is the weight of the background ensemble perturbation and is set to 0.5 following (Zhang et al. 2004). We applied additional inflation every 5 min to further increase the ensemble spread. This additional inflation is realized by scaling the spread of θ to 2 K in the areas influenced by observational data in the filter updating. This procedure has an effect of increasing the spread of thermal variables and limits additional uncertainties to the areas impacted by observations; it has a similar effect as the additive noise method of (Dowell and Wicker 2009) where temperature perturbations are only added in areas of precipitation.

For spatial localization a fifth-order correlation function (Gaspari and Cohn 1999) is used. The horizontal radius is set to 8 km and the vertical radius is 4 km. The model variables updated by data assimilation system include the grid point values of wind components u , v , w , potential temperature θ , perturbation geopotential ϕ , water vapor mixing ratio q_v , and mixing ratios of microphysical variables q_r , q_i , q_s , and q_g for rain, ice, snow and graupel. Both radial velocity V_r and radar reflectivity Z are assimilated.

For iEnSRF, the time interval between t_{n-1}^* and t_n is set to 4 minutes for the first analysis (at 25 min) and 3 minutes for all subsequent analysis cycles. In RIP, the number of iterations is automatically adjusted according to a criterion based on the mean squares observation minus forecast or the forecast innovation. A similar criterion is not appropriate in our case, because none of the model state variables are directly observed, and a good fit of model state to observations does not guarantee accurate state estimation. We choose instead to set the number of iterations to 3 for all analysis cycles with iterations, which is consistent with the experience of (Kalnay and Yang 2010). In our iterative pro-

cedure, spatial covariance inflation and localization configurations for updating the state at t_{n-1}^* are the same as those for updating state at t_n . Temporal localization is performed using a fifth-order correlation function (Gaspari and Cohn 1999). The cutoff radius of the temporal localization is set to 6 minutes (slightly long than a radar volume scan time).

3.4. OSSE design

As in many earlier OSSE studies with EnKF (e.g. Tong and Xue 2005; Zhang et al. 2006), we first examine iEnSRF with a perfect model and a storm environment defined by the correct sounding. In this perfect model situation, two experiments are performed. One is named EnSRF_ne, using EnSRF, while the other is iEnSRF_ne, using iEnSRF. The “ne” in the names indicates no model or environmental error. Following (Tong and Xue 2005) and (Xue et al. 2006), we perform analyses every 5 minutes, from 25 min to 90 min for both experiments. Short-range deterministic forecasts are launched from the ensemble mean analyses at 40 min and 60 min, respectively. The forecasts launched at 40 min are designed to determine the impact of iEnSRF on forecasts with a short assimilation window while the forecasts launched at 60 min examine the impact of iEnSRF after more data are assimilated through additional cycles.

In a second set of experiments, both EnSRF and iEnSRF are subject to a more realistic condition that includes error in both the prediction model and storm environment. Two experiments are again performed, EnSRF_e and iEnSRF_e, where “e” refers to the fact that error is included in the model and environmental sounding. As in the error-free experiments, cycled analyses are performed from 25 min to 90 min at 5 minute intervals and two deterministic forecasts are launched from ensemble mean analyses at 40 min and 60 min. Similar to (Zhang and Meng 2007) and (Snook et al. 2011), the model error or

uncertainty is modeled by using different physical parameterization schemes from those used in the truth simulation. Specifically, the Smagorinsky first-order closure scheme (SFOC) instead of the 1.5-order turbulent-kinetic energy (TKE) scheme is used for the subgrid-scale turbulence parameterization; the Purdue Lin (Lin et al. 1983; Rutledge and Hobbs 1984) instead of WSM6 scheme is used for microphysics, and a 2nd-order instead of a 3rd-order Runge-Kutta scheme is used for model time integration. The environmental error is introduced by adjusting the profile of water vapor mixing ratio (q_v) and lapse rate of temperature of the sounding. A coefficient of 0.9 is multiplied to the q_v profile to represent an underestimate of the environmental moisture. For temperature, the amplitude of perturbation from the original profile mean is first reduced by 10%, a constant is then added to the profile so that its surface value remains unchanged. The adjusted sounding is shown in Fig. 2 (gray lines). The largest differences in this modified sounding are the smaller value of CAPE, higher lifting condensation level (LCL), and larger dew point depression at the lower levels, indicating a less convectively unstable environment.

The impact of data assimilation using the iEnSRF is then examined in terms of both analysis and forecast errors. In order to isolate the effects of the difference in the initial condition, we use the perfect model for the free-forecast period of both error-free and error-containing experiments. The configurations of model and data assimilation for all four experiments discussed above are listed in Table 1, including the parameterization schemes, assimilation window length, and the localization and inflation configurations.

4. Results and discussions

The root-mean square (RMS) errors of analyzed model state variables are used to quantify and compare the performance of iEnSRF and standard EnSRF. Following (Tong

and Xue 2005) and (Xue et al. 2006), the RMS errors are calculated against the truth at grid points where the truth reflectivity is greater than 10 dBZ. The mass field used for verification is the perturbation geopotential height in meters. Meanwhile, for quantitative comparison of iEnSRF and EnSRF, we define the improvement produced by iEnSRF, Imp , as the percentage difference,

$$Imp = 100 \times (e_{ensrf} - e_{iensrf}) / e_{ensrf} ,$$

where e is the RMS error while the subscript denotes the analysis scheme used. Note that a positive value of Imp represents an improvement in the analysis of iEnSRF.

4.1. Results with no model or environmental error

Figure 4 compares the RMS errors from the EnSRF_ne and iEnSRF_ne. When used from 25 min to 90 min, iEnSRF generally performs better than regular EnSRF in the first 4 – 5 cycles but its errors gradually become comparable with or even worse than those of EnSRF in later cycles. It can be seen in Figure 4 that iEnSRF reduces the initial background error for all variables except for q_v more than EnSRF does at the end of the first analysis cycle at 25 min. Table 2 shows that the Imp for the three wind components, u , v , and w , is between 8.6% and 14.4% at this time. For variables that are not directly related to radial velocity, such as geopotential height ϕ and potential temperature θ , the Imp is 34.4% and 14.6%, respectively. For the hydrometeor variables, the Imp is somewhat less. For q_v , the Imp is -62% in the first cycle (Table 2). This suggests that the ensemble covariances used to update the moisture and microphysical variables are not reliable at the end of the first cycle even with the iterations of iEnSRF.

At 40 min, after 4 assimilation cycles, the errors in both EnSRF_ne and iEnSRF_ne are greatly reduced from their initial levels. The analysis errors for the wind

components in EnSRF_e are about 2.5 m s^{-1} while those in iEnSRF_e are reduced to about 2.0 m s^{-1} (Fig. 4), representing an *Imp* of more than 20% for u and v and 30% for w by iEnSRF. Although the analysis error of ϕ in iEnSRF_ne is not much smaller than that in EnSRF_ne, the analysis error of θ in the former is about 31.16% smaller than that in the latter. Moreover, substantial improvement can be seen for hydrometeor variables after applying iEnSRF for 4 cycles. The *Imp* for the analysis error of q_v is about 8.5% while those for q_r , q_s , and q_g are all over 30%. This result suggests that the iterations improved not only state estimation but also the covariance estimation, since microphysical variables depend strongly on the cross-variable covariance when they are updated by radial velocity observations.

However, the positive impact of the iterative procedure did not last through the remainder of the assimilation cycles. This is most clearly seen in the analysis and background forecast errors of θ in the later cycles (Fig. 4). From 75 through 90 min, the errors of iEnSRF are noticeably larger. The same degradation is seen for the wind components. This result agrees with (Kalnay and Yang 2010), who also found that performing additional iterations after the filter reaches its asymptotic level could lead to larger analysis errors. This is due to over-fitting of the analysis to observations, when the observations are used repeatedly after reasonable state and covariance estimations have already been established.

It is therefore recommended that the iterative procedure is stopped after the DA system stabilizes, i.e., when the analysis errors calculated against the observation level off. Through further tuning and sensitivity experiments it may be possible to automatically determine when this stabilization has occurred; the extra iteration step should then be

halted.

Launching from the analyses at 40 min, the forecast errors in EnSRF_ne (grey dash lines in Figure 4) increase rapidly and became about twice as large by 90 min for most variables. In contrast, the forecast errors in iEnSRF_ne (dark dash lines in Figure 4) grow more slowly and remain substantially lower than those of EnSRF_ne throughout the forecast period. For instance, the improvement over EnSRF is between 27 and 35% for u , v , and w at 90 min while improvement for other variables is at least 18% (Table 2). This is true even for variables that are not directly related to radial velocity or reflectivity, such as ϕ , θ , and q_v . It is interesting to note that even though the improvement to the analysis at 40 min is slightly negative for ϕ , the forecast error in ϕ starting from this analysis is improved by close to 32% by 90 min, due to a more accurate analysis of most other state variables positively impacting the evolution of the forecast.

As mentioned earlier, we also launched deterministic forecasts from ensemble mean analyses at 60 min. By this time, both EnSRF and iEnSRF had reached their asymptotic error levels and the analysis errors of all variables in EnSRF_ne were comparable with those in iEnSRF_ne. It can be seen in Figure 4 that the forecast error curves (dash lines) for these two experiments were nearly identical after being launched at 60 min, indicating that applying iterations after the filter reaches its asymptotic error level (shortly after 40 min in this case) does not improve the analysis and subsequent forecast. At 90 min, the forecast errors for nearly all variables in iEnSRF_ne become slightly larger than those in EnSRF_ne. Meanwhile, at 90min, the error level of the forecast in iEnSRF_ne starting from 40 min is comparable with that of forecast starting from 60 min. This suggests that applying iEnSRF effectively increases the forecast lead time by 20

minutes in the current case; in other words, the assimilation window can be 20 minutes shorter to reach a similar quality of state estimation for the current supercell storm, so that forecasts can be issued 20 minutes earlier.

4.1. Results with model and environmental errors

A perfect prediction model and perfect environmental conditions are not possible for real data assimilation problems. In this section, we examine results the second set of experiments; those that include prediction model and storm environment errors. Figure 5 shows the RMS errors from experiments EnSRF_e and iEnSRF_e. In this more realistic scenario, iEnSRF still produces more accurate analyses than EnSRF in the first several cycles. Similar to the no error case, the RMS errors in the later cycles become comparable to those of EnSRF. Overall, the analysis errors in the error-containing experiments are comparable with the corresponding error-free experiments (compare Figure 5 to Figure 4). As can be seen in

Table 3, the iteration procedure in iEnSRF has positive impacts on the wind analysis at the end of the first cycle but the relative improvement is less than 10%, which is about 22-32 % smaller than that in no-error experiments. The *Imp* for ϕ and θ are also smaller, achieving 22.66% and 8.52%, respectively, compared to the 34% and 14% of no-error case. Among water vapor and hydrometeors, iEnSRF produces smaller errors for q_r and q_g but it produces a large degradation in q_s versus q_v as in the no-error case. Similar to the no error case, this larger analysis error for q_s here is likely due to unreliable covariance associated with the microphysical variables, and such a problem can be enlarged by the use of a wrong microphysical scheme.

By 40 min or after 4 assimilation cycles, the improvements by iEnSRF are again evident. At this time, the improvements to u , v , and w are between 28% and 44% and the improvement to ϕ is also substantial (21.47%). The improvement to θ is smaller in iEnSRF_e than in iEnSRF_ne (4.87 versus 31.16%), this is believed to be related to the error in the environment. The improvements to the moisture and hydrometeor variables are clearly evident, except for a small degradation in q_s . On average, the improvements to the hydrometeors are smaller than the no-error case. Similar to the no-error case, the analysis errors of iEnSRF in later cycles become close to those of EnSRF analyses, again suggesting that further iterations are unnecessary and may be undesirable after an asymptotic error level is reached..

When forecasts are launched at 40 min, the forecast errors in EnSRF_e and iEnSRF_e initially grow at similar rates as the corresponding no-error runs (compare Figure 5 to Figure 4), but after 10-15 min the errors grow much faster, reaching substantially higher levels by 90 min. These large forecast errors can be attributed to errors in the storm environment that cannot be easily corrected by the radar data. Throughout the forecast period, the RMS errors of iEnSRF_e remain lower than those of EnSRF_e for most variables. For a few variables, e.g., u , v , and q_s , the *Imp* is larger than it was at 40 min, indicating that the benefit of the iterative procedure, in this error-containing case (as well as the error-free case, Figure 4), is retained or even amplified for at least 50 min in the forecast period.

By 60 min, the analysis errors in both EnSRF_e and iEnSRF_e have leveled off and the differences between them, though still identifiable, have become rather small. As a result, forecasts launched from analyses at this time produce similar forecast errors be-

tween iEnSRF_e and EnSRF_e (Figure 5), although those of iEnSRF_e are still slightly smaller. Compared to the error-free case, it seems to be beneficial to apply the iteration procedure for a couple more cycles in the error-containing case, given that Imp is mostly positive for 90minF60 in the error case (Table 3) while the corresponding Imp in the error-free case is mostly negative (Table 2). It is observed that the analysis errors for u and w at 60 min is still clearly lower in iEnSRF_e than those in EnSRF_e while the differences is already very small between iEnSRF_ne and EnSRF_ne by this time; further iterations in the latter case would start to hurt. Overall, the benefit of using the iterative procedure to reduce spin-up time in iEnSRF is clear in both error-free and error-containing experiments.

4.3. Error correlation structures, and analysis and forecast fields

To help understand how the iterations produce the positive impacts noted in the previous subsection, we examine the background error correlation coefficients within the first assimilation cycle of EnSRF_e and iEnSRF_e (Figure 6). The correlation between w and θ is first examined. A positive correlation between w and θ perturbations due to latent heat release within the updraft regions is physically consistent with and important for deep moist convection. In a vertical cross-section through the main updraft, one sample point marked by a red triangle is selected, where a hypothetical radial velocity (V_r) observation is assumed. At this point, the estimated w is smaller than the truth in both Figs.6a and 6b. Therefore, if a V_r observation from a nearby radar can correct w at sampled point, the increment of w at this point is expected to be positive. Surrounding this point, the initial estimate of θ was also smaller than the truth (Figure 6a), implying a positive correlation between θ and w around the point is necessary in order for the assimilation of V_r to

produce a positive θ increment, thereby reducing its error through variable cross-correlation. However, the correlation coefficients calculated from the ensemble background forecasts in EnSRF_e are negative within the red ellipse (a region within the localization radius of the V_r observation) at this time (Figure 6a). Therefore, using the covariance between θ and the w component in radial wind prior to update θ will lead to negative impact on the θ analysis. Conversely, in Figure 6b for iEnSRF, the correlations calculated from the background ensemble forecasts after three iterations are generally positive within the ellipse. This indicates that positive error correlations between θ and w are corrected captured by the ensemble after 3 iterations in iEnSRF, but not in EnSRF.

Similar behaviors can be observed with the q_g and w fields. Near the hypothetical observation point (marked by triangle), the forecast q_g and w in both EnSRF_e and iEnSRF_e are smaller than the truth values (Figure 6c, d). Within the ellipse, positive correlations between q_g and w can be correctly estimated from the forecast ensembles in both EnSRF_e and iEnSRF_e, but the maximum correlation coefficient in the former is small, reaching only 0.2, while in the latter, the value reaches 0.6. Given the larger correlation coefficient in iEnSRF_e, the filter can produce a larger correction to q_g through the assimilation of V_r observations. In addition to the magnitude of error correlation, its spatial distribution is more reasonable in iEnSRF_e. The error maximum of q_g in iEnSRF_e is located near the bottom boundary of ellipse, implying that the error correlation should be smaller near the triangle while larger near the error maximum. This tendency is well captured in iEnSRF_e. In EnSRF_e, this spatial distribution is incorrectly estimated, with the error correlation maximum located near the triangle.

To further explore the impact of the iteration procedure on the analyzed storm, we examine the wind and q_g fields at 40 min, the time when we launch the first set of forecasts (Figure 7). As mentioned in section 3.1, the storm in the truth simulation begins to split into two cells (NC and SC mentioned in section 3.1) at 40 min. The differences between the vertical profiles of analysis errors (not shown) of iEnSRF_e and EnSRF_e were found to be substantial in the mid and upper troposphere, especially for w and q_g . For example, at 5 km AGL, it is clear that there are two updraft maxima in the truth simulation (Figure 7a). This structure is captured in both EnSRF_e and iEnSRF_e. However, the updrafts and precipitation core are stronger in iEnSRF_e (Figure 7c), closer to the truth, than in EnSRF_e (Figure 7b). The updraft of the northern cell in EnSRF_e is particularly weak. In the truth simulation, the region of q_g greater than 2 g kg^{-1} extends to $x=45 \text{ km}$, which is not well captured by EnSRF_e but better in iEnSRF_e. These findings are consistent with the fact that the storm in EnSRF_e is less well spun-up through the limited number of assimilation cycles without iterations.

Looking higher in the storm, at 10 km AGL, there is indication of cell splitting in the structure of the updraft in the truth simulation (Figure 7d). In EnSRF_e (Figure 7e), only a single updraft core is identifiable while iEnSRF_e produces an updraft structure (Figure 7f) that is closer to the truth. These results again show the benefit of iterations in accelerating the storm spin up.

At the end of 50-min forecast, the forecast errors of both iEnSRF_e and EnSRF_e have become large (Figure 5), but the errors of iEnSRF_e are still smaller than those of EnSRF_e (Table 3). To see the visual differences in the forecasts, Figure 8 shows the forecast fields at 90 min from EnSRF_e and iEnSRF_e at 5 and 10 km AGL. At this time,

the strength of storm in both EnSRF_e and iEnSRF_e is weaker than the truth simulation, especially in terms of graupel mixing ratio (q_g). As suggested earlier, the less unstable sounding that is used to define the storm environment likely contributed to such forecast errors. Nonetheless, the forecast storm in iEnSRF_e is somewhat stronger than that in EnSRF_e. For example, at 5 km AGL, the areal extent and maximum value of q_g associated with SC are larger in iEnSRF_e than those in EnSRF_e. We see similar trends at 10 km AGL with a larger updraft and area of q_g in iEnSRF_e than in EnSRF_e. Comparison with the truth simulation shows that the stronger and larger updraft of iEnSRF_e is more accurate than that of EnSRF_e. Therefore, the smaller error in iEnSRF_e corresponds to more accurate forecast of storm strength. Overall, although the relative improvement yielded by iEnSRF in the presence of model and environment error is not as large as that with perfect conditions, the benefits the iteration procedure in iEnSRF short-range storm forecasting through accelerated error reduction in the state estimation is clear.

5. Summary and conclusions

An iterative procedure based on the ensemble square root filter (EnSRF), which we refer to as iEnSRF, is designed with the goal of accelerating the “spin-up” of ensemble Kalman filter state estimation. The procedure is designed to be used in situations in which the first guess ensemble has a poor mean state estimate and poor ensemble error covariances. This procedure is similar to the “running-in-place” (RIP) procedure proposed by (Kalnay and Yang 2010) but differs substantially in implementation due to differences between the local ensemble transform Kalman filter (LETKF) and the EnSRF algorithms used in the respective systems. In iEnSRF, the background states at the analysis time and at an earlier time are combined into a new extended state vector. With this

extended vector, the states at both times are updated by the filter, using the asynchronous ensemble Kalman filter (Sakov et al. 2010). By launching ensemble forecasts from the earlier updated states, and using the forecasts as the new background ensemble in Kalman filter updating in subsequent iterations within the same cycles, additional information can be extracted from the observations to more rapidly reach a more accurate state estimate.

Specifically, the iEnSRF contains three steps: First, a backward EnSRF analysis is performed that updates the ensemble model states at an earlier time. Second, an ensemble of forecasts is run from these updated model states to the analysis time. These two steps are then repeated a predetermined number of times. The backward analysis is performed via asynchronous EnKF which can use observations not collected at the state updating time.

We test the iEnSRF algorithm using simulated radar data for an idealized super-cell storm. Two sets of experiments are performed; one employs a perfect prediction model and a storm environment defined by the true environmental sounding. The other experiment set includes a combination of prediction model error and environmental error. In the error-free case, iEnSRF accelerates the rate of error reduction and reaches a lower error level within the first 4 cycles. Continued application of the iterative procedure in later cycles leads to larger errors than in the non-iterative case, suggesting over-fitting of the analysis to observations. In this idealized scenario, the error of the deterministic forecast starting from iEnSRF analysis obtained after 4 cycles is found to be substantially smaller than that starting from EnSRF analysis valid at the same time. After both iEnSRF and EnSRF reach their asymptotic error level (~8 cycles), the difference between analyses and subsequent forecasts yielded by these two methods became small.

When model error and environmental error are present, the results are very similar. iEnSRF performs better than EnSRF in the first 4 cycles and becomes comparable in later cycles. The relative improvement over the non-iterative case is somewhat less than the error-free case but is still clearly evident. Examination of the analyzed storm at 40 min, or after 4 assimilation cycles, indicates that iEnSRF is able to capture the storm splitting, intensity, and structure better than EnSRF. The benefit of the improved analysis is maintained throughout the 50 min forecast launched from the ensemble mean analysis at 40 min.

To better understand how iEnSRF is able to produce more accurate analyses in the first few cycles, we examined the background error correlations between different variables in the first cycle. Results showed that the error correlations calculated from the ensemble after 3 iterations with iEnSRF are more physically consistent than those obtained without iterations. The improved ensemble error covariance obtained by the iterative procedure helps with not only just with the analysis of the wind field, but also with the estimation of state variables, such as temperature, humidity, and microphysical variables that are not directly linked (through the observation operator) to the assimilated radial velocity observations. Through iterations, iEnSRF is able to reach a constant level of state estimation error in a fewer number of cycles than the corresponding non-iterated version.

Similar to the findings of (Kalnay and Yang 2010), the iterative procedure is found to dramatically improve state estimation in the first few assimilation cycles when starting from a poor initial ensemble. Such a poor initial ensemble is generally the case in thunderstorm initialization, where useful radar observations are typically not available

before precipitation is present within a developing thunderstorm, or when data assimilation is not running continuously in time so that ongoing thunderstorms have to be spun-up starting from coarse resolution operational model background that has little or no knowledge about the ongoing thunderstorms. After the data assimilation cycles stabilize and the analysis error levels off, it is neither necessary nor desirable to continue the iterations, because over-fitting to observations can occur and iterations also incur additional computational costs. For the problem of assimilating radar volume scan data at about 5 minute intervals, it is recommended to use iEnSRF only in the first 4-5 cycles. For practical implementations, we expect some level of tuning to reach optimal configurations. Future work will examine the application of iEnSRF for real data cases.

Acknowledgments This research was primarily supported by NSF grants OCI-0905040 and AGS-0802888. The second author was also supported by NSF grants AGS-0941491, AGS-1046171, and AGS-1046081. Computations were carried out at the University of Oklahoma Supercomputer Center for Education and Research (OSCER), and on the CAPS Linux Cluster machines.

References

- Anderson JL, 2001. An ensemble adjustment Kalman filter for data assimilation. *Monthly Weather Review*, **129**: 2884-2903.
- Anderson JL, Collins N, 2007. Scalable implementations of ensemble filter algorithms for data assimilation. *J Atmos Ocean Tech*, **24**: 1452-1463.
- Caya A, Sun J, Snyder C, 2005. A comparison between the 4D-VAR and the ensemble Kalman filter techniques for radar data assimilation. *Mon. Wea. Rev.*, **133**: 3081–3094.
- Crook NA, Dowell D, Sun J, Zhang Y, 2004: Assimilation of radar observations of a supercell storm using 4DVar: Parameter retrieval experiments. *22nd Conference on Severe Local Storms*, Hyannis, Massachusetts, Amer. Meteor. Soc., CDROM 8A.2.
- Dowell DC, Wicker LJ, 2009. Additive noise for storm-scale ensemble data assimilation. *J. Atmos. Oceanic Technol.*, **26**: 911-927.
- Evensen G, 1994. Sequential data assimilation with a nonlinear quasi-geostrophic model using Monte Carlo methods to forecast error statistics. *J. Geophys. Res.*, **99**: 10143-10162.
- Evensen G, 2003. The ensemble Kalman filter: Theoretical formulation and practical implementation. *Ocean Dynamics*, **53**: 343-367.
- Gaspari G, Cohn SE, 1999. Construction of correlation functions in two and three dimensions. *Q J Roy Meteor Soc*, **125**: 723-757.
- Houtekamer PL, Mitchell HL, 2001. A sequential ensemble Kalman filter for atmospheric data assimilation. *Mon. Wea. Rev.*, **129**: 123-137.

- Hunt BR, Kostelich EJ, Szunyogh I, 2007. Efficient data assimilation for spatiotemporal chaos: A local ensemble transform Kalman filter. *Physica D: Nonlinear Phenomena*, **230**: 112-126.
- Jung Y, Xue M, Zhang G, Straka J, 2008. Assimilation of simulated polarimetric radar data for a convective storm using ensemble Kalman filter. Part II: Impact of polarimetric data on storm analysis. *Mon. Wea. Rev.*, **136**: 2246-2260.
- Kalnay E, Yang SC, 2010. Notes and Correspondence Accelerating the spin-up of Ensemble Kalman Filtering. *Q J Roy Meteor Soc*, **136**: 1644-1651.
- Kalnay E, Li H, Miyoshi T, Yang SC, Ballabrera-Poy J, 2007. Response to the discussion on "4-D-Var or EnKF?" by Nils Gustafsson. *Tellus A*, **59**: 778-780.
- Klemp JB, 1987. Dynamics of Tornadic Thunderstorms. *Annu Rev Fluid Mech*, **19**: 369-402.
- Lin Y-L, Farley RD, Orville HD, 1983. Bulk parameterization of the snow field in a cloud model. *J. Climat. Appl. Meteor.*, **22**: 1065-1092.
- Rutledge SA, Hobbs PV, 1984. The mesoscale and microscale structure and organization of clouds and precipitation in midlatitude cyclones. Part XII: A diagnostic modeling study of precipitation development in narrow cold-frontal rainbands. *J. Atmos. Sci.*, **41**: 2949-2972.
- Sakov P, Evensen G, Bertino L, 2010. Asynchronous data assimilation with the EnKF. *Tellus A*, **62**: 24-29.
- Skamarock WC, Klemp JB, Dudhia J, Gill D, Barker D, Wang W, Powers JG, 2005: A description of the Advanced Research WRF Version 2. NCAR Technical Note NCAR/TN-468+STR.

- Snook N, Xue M, Jung YS, 2011. Analysis of a Tornadic Mesoscale Convective Vortex Based on Ensemble Kalman Filter Assimilation of CASA X-Band and WSR-88D Radar Data. *Monthly Weather Review*, **139**: 3446-3468.
- Snyder C, Zhang F, 2003. Assimilation of simulated Doppler radar observations with an ensemble Kalman filter. *Mon. Wea. Rev.*, **131**: 1663-1677.
- Tong M, Xue M, 2005. Ensemble Kalman filter assimilation of Doppler radar data with a compressible nonhydrostatic model: OSS Experiments. *Mon. Wea. Rev.*, **133**: 1789-1807.
- Weisman ML, Klemp JB, 1982. The dependence of numerically simulated convective storms on vertical wind shear and buoyancy. *Mon. Wea. Rev.*, **110**: 504-520.
- Whitaker JS, Hamill TM, 2002. Ensemble data assimilation without perturbed observations. *Mon. Wea. Rev.*, **130**: 1913-1924.
- Xue M, Tong M, Droegemeier KK, 2006. An OSSE framework based on the ensemble square-root Kalman filter for evaluating impact of data from radar networks on thunderstorm analysis and forecast. *J. Atmos. Ocean Tech.*, **23**: 46-66.
- Xue M, Jung YS, Zhang GF, 2010. State estimation of convective storms with a two-moment microphysics scheme and an ensemble Kalman filter: Experiments with simulated radar data. *Q J Roy Meteor Soc*, **136**: 685-700.
- Yang SC, Corazza M, Carrassi A, Kalnay E, Miyoshi T, 2009. Comparison of Local Ensemble Transform Kalman Filter, 3DVAR, and 4DVAR in a Quasigeostrophic Model. *Monthly Weather Review*, **137**: 693-709.

- Yussouf N, Stensrud DJ, 2010. Impact of Phased-Array Radar Observations over a Short Assimilation Period: Observing System Simulation Experiments Using an Ensemble Kalman Filter. *Monthly Weather Review*, **138**: 517-538.
- Zhang F, Snyder C, Sun J, 2004. Impacts of initial estimate and observations on the convective-scale data assimilation with an ensemble Kalman filter. *Mon. Wea. Rev.*, **132**: 1238-1253.
- Zhang F, Meng Z, Aksoy A, 2006. Tests of an ensemble Kalman filter for mesoscale and regional-scale data assimilation. Part I: Perfect model experiments. *Mon. Wea. Rev.*, **134**: 722–736
- Zhang FQ, Meng ZY, 2007. Tests of an ensemble Kalman filter for mesoscale and regional-scale data assimilation. Part II: Imperfect model experiments. *Monthly Weather Review*, **135**: 1403-1423.
- Zhang S, Rosati A, 2010. An inflated ensemble filter for ocean data assimilation with a biased coupled GCM. *Mon. Wea. Rev.*, **138**: 2010:doi: 10.1175/2010MWR3326.1.

Table 1. The model and data assimilation configurations of OSSEs

Experiment name	EnSRF_ne	iEnSRF_ne	EnSRF_e	iEnSRF_e
Analysis scheme	EnSRF	iEnSRF	EnSRF	iEnSRF
Iteration interval time (min)	N/A	cycle one: 4 other cycles: 3	N/A	cycle one: 4 other cycles: 3
Iteration number for each cycle	N/A	3	N/A	3
Temporal localization (min)	N/A	6	N/A	6
Parameterization schemes for analysis	RK3/ WSM6/ TKE		RK2/ Lin /SFOC	
Parameterization schemes for forecast	RK3/ WSM6/ TKE			
Environmental sounding	Truth	Truth	Adjusted	Adjusted
Spatial Localization radius (km)	Horizontal: 8 km / Vertical: 4 km			
Inflation scheme/coefficient	Relaxation / 0.5			
Additional inflation	Rescaling spread to 2 K for θ			

Table 2. Percentage differences between RMS errors of iEnSRF_ne and EnSRF_ne at 25, 40 and 90 min of model time. At 25 and 40 min, the errors are for the analyses while at 90 min they are for forecasts. Positive values mean that errors are smaller in iEnSRF_ne while negative ones mean errors are larger in iEnSRF_ne. F40 represents forecast proceeding from 40 min while F60 represents forecast proceeding from 60 min.

Time	u	v	w	ϕ	θ	q_v	q_r	q_s	q_g
25min	13.80	8.65	14.42	34.41	14.60	-62.00	16.11	4.65	4.57
40min	22.87	26.53	32.82	-1.48	31.16	8.51	32.20	31.21	33.21
90minF40	27.32	34.63	27.02	31.29	18.35	25.40	19.56	28.40	39.15
90minF60	-4.44	-15.17	-19.50	-9.50	-6.47	-3.03	-30.02	-0.20	-8.16

Table 3. Percentage differences between RMS errors of iEnSRF_e and EnSRF_e at 25, 40 and 90 min of model time. At 25 and 40 min, the errors are for the analyses while at 90 min they are for forecasts. F40 represents forecast proceeding from 40 min while F60 represents forecast proceeding from 60 min.

	u	v	w	ϕ	θ	q_v	q_r	q_s	q_g
25min	9.07	5.33	8.50	22.66	8.52	-1.16	2.08	-86.79	4.53
40min	28.63	32.79	44.26	21.47	4.87	9.12	13.09	-2.72	23.40
90minF40	14.39	15.75	12.71	13.36	5.81	9.05	13.55	16.16	19.04
90minF60	11.36	-0.73	12.64	-0.20	5.39	4.16	9.54	7.36	3.90

List of figures

Figure 1. The Flow chart for EnSRF and iEnSRF procedure in each cycle, where the t_{n-1}^* is an arbitrarily intermediate time between t_{n-1} and t_n .

Figure 3. The original (black) and modified (gray) environmental soundings using by the truth simulation, and by the error-containing OSSEs, respectively. Solid and dashed lines are for temperature and dewpoint temperature, respectively. LCL:M indicates the LCL of modified sounding while LCL:T indicates the original LCL.

Figure 4. The graupel mix ratio (shaded), vertical velocity (contour at interval of 4 m s^{-1}) and horizontal wind (vector) at 5km AGL for the truth simulation at model times of (a) 40 min and (b) 90 min. red dot indicates the location of initial thermal bubble.

Figure 5. The evolution of RMS errors for experiments EnSRF_ne (grey line) and iEnSRF_ne (black line). Solid lines represent errors within the assimilation window while dash lines stand for errors of deterministic forecasts launched from the ensemble mean analyses at 40 and 60 minutes.

Figure 6. The same as Figure 4, but for experiments EnSRF_e (grey line) and iEnSRF_e (black line).

Figure 7. Vertical cross sections of forecast errors, calculated as the ensemble mean minus the truth (error field shaded with vertical velocity error shown as vertical vectors), and the correlation coefficients of forecast errors (contours at intervals of 0.2), at 25 min, the time of first analysis, in an x-y plane at y=30 km. The 0.2 correlation contours are in bold. The red ellipse is the 0.2 contour for the

localization coefficient for the observation located at the red triangle. For iEnSRF_e the forecasts are at the end of the third iteration. The upper panels show the forecast errors of θ (shaded) and w (vertical vectors) and forecast error correlation coefficient between w at the point marked by the red triangle and θ at the grid point, for EnSRF_e (left) and iEnSRF_e (right). The lower panels are the same as the upper panels except θ is replaced by q_g .

Figure 8. The graupel mix ratio (shaded), vertical velocity (contoured at intervals of 4 m s^{-1}) and horizontal wind vectors at 40 min. for the truth simulation (left), EnSRF analysis (middle) and iEnSRF_e analysis (right), at 5 km (upper panels) and 10 km (lower panels) AGL. w contours are shown in bold.

Figure 9. The same as Figure 7, but for deterministic forecasts at 90 min starting from the ensemble mean analyses at 40 min. in EnSRF_e (mid panels) and iEnSRF_e (right panels), as compared to the truth (left panels).

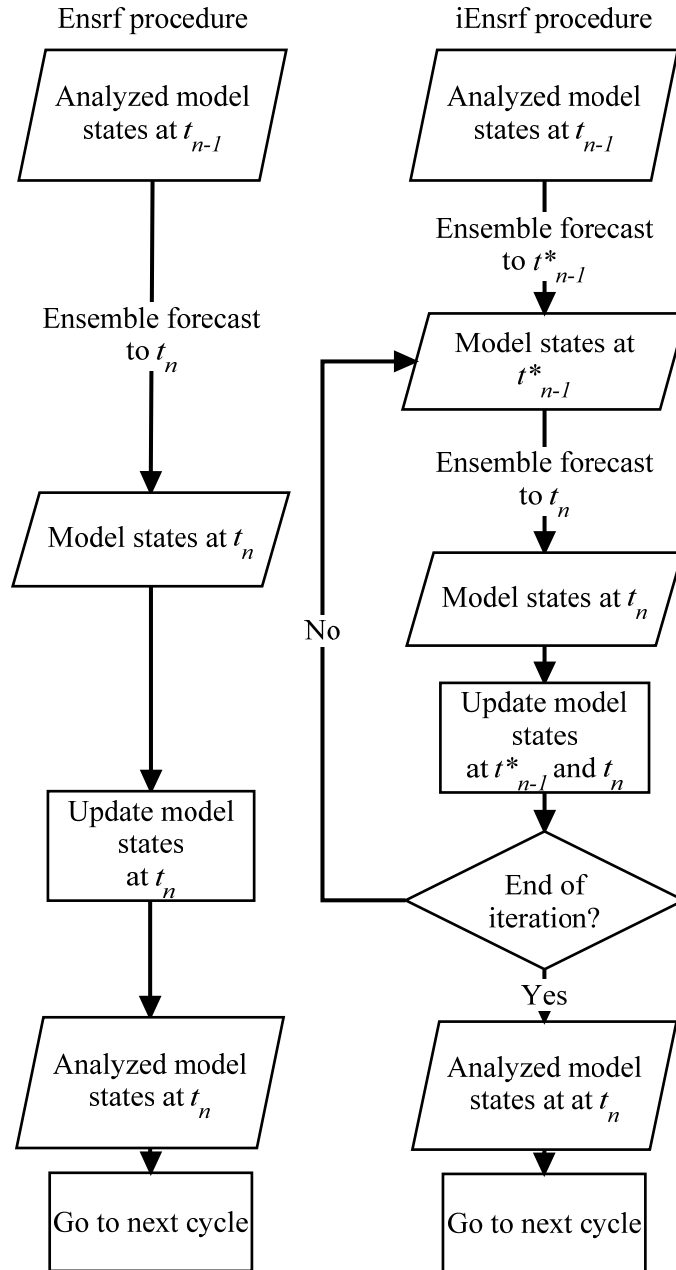


Figure 1. The Flow chart for EnSRF and iEnSRF procedure in each cycle, where the t_{n-1}^* is an arbitrarily intermediate time between t_{n-1} and t_n .

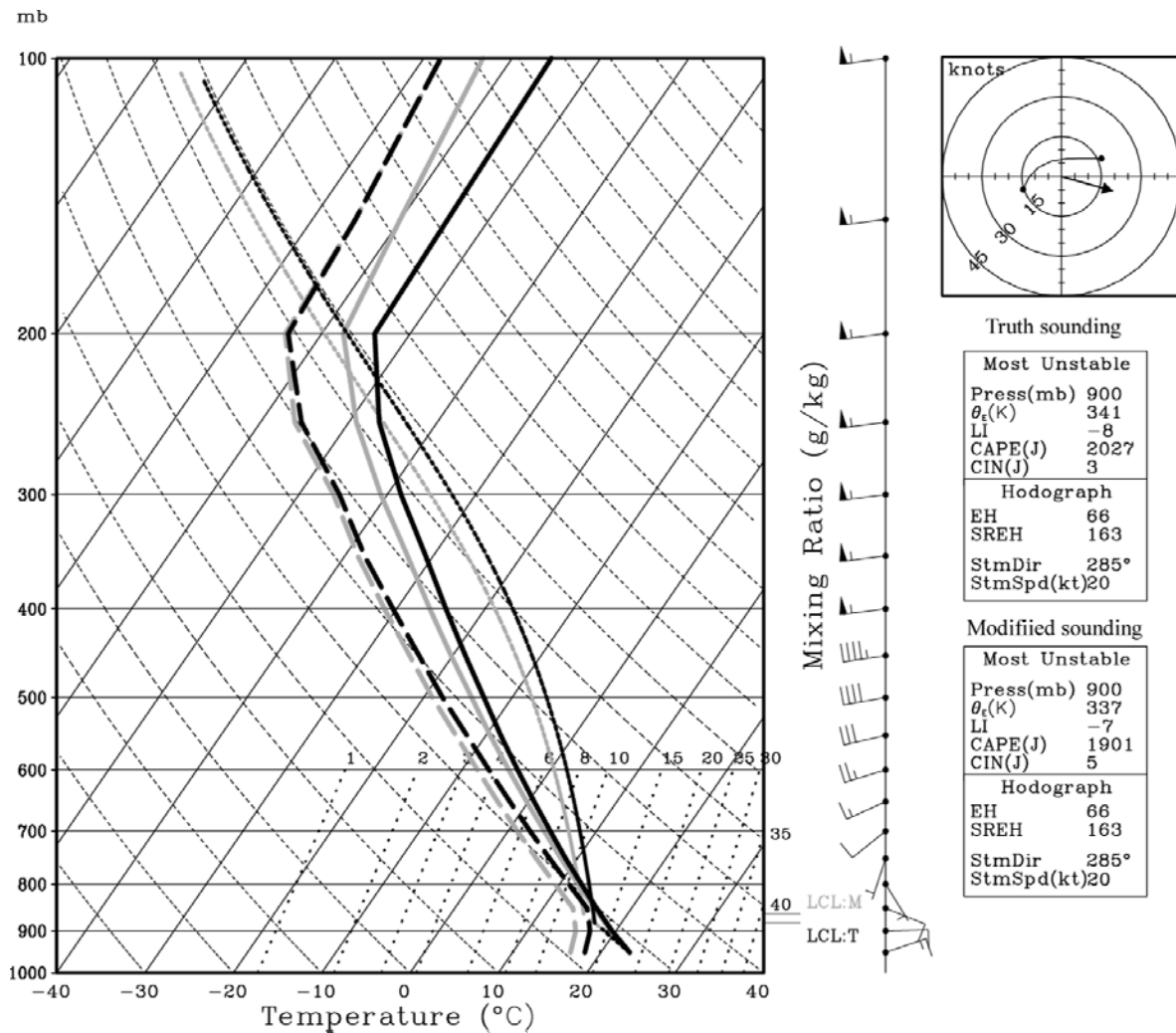


Figure 2. The original (black) and modified (gray) environmental soundings using by the truth simulation, and by the error-containing OSSEs, respectively. Solid and dashed lines are for temperature and dewpoint temperature, respectively. LCL:M indicates the LCL of modified sounding while LCL:T indicates the original LCL.

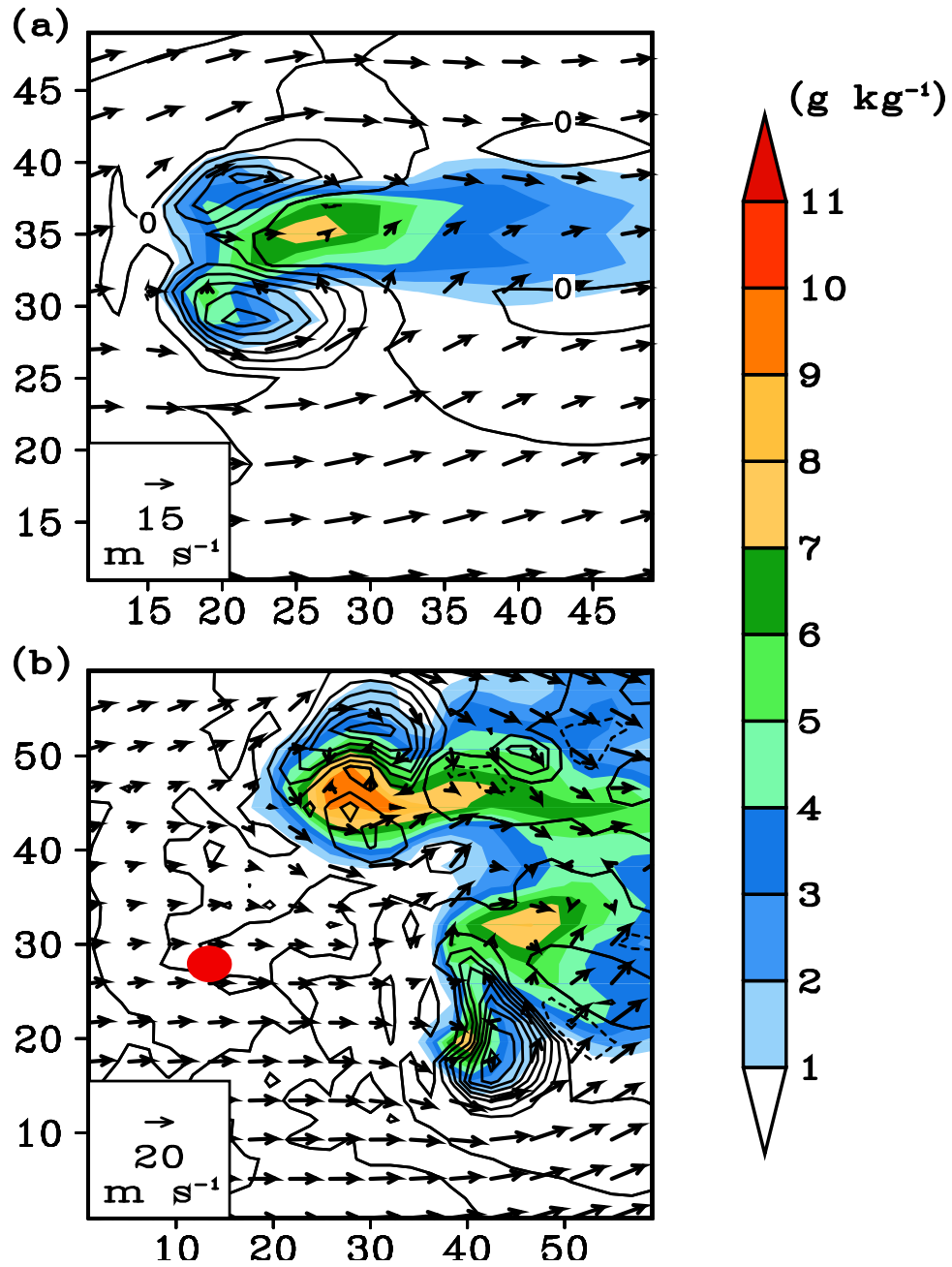


Figure 3. The graupel mix ratio (shaded), vertical velocity (contour at interval of 4 m s^{-1}) and horizontal wind (vector) at 5 km AGL for the truth simulation at model times of (a) 40 min and (b) 90 min. red dot indicates the location of initial thermal bubble.

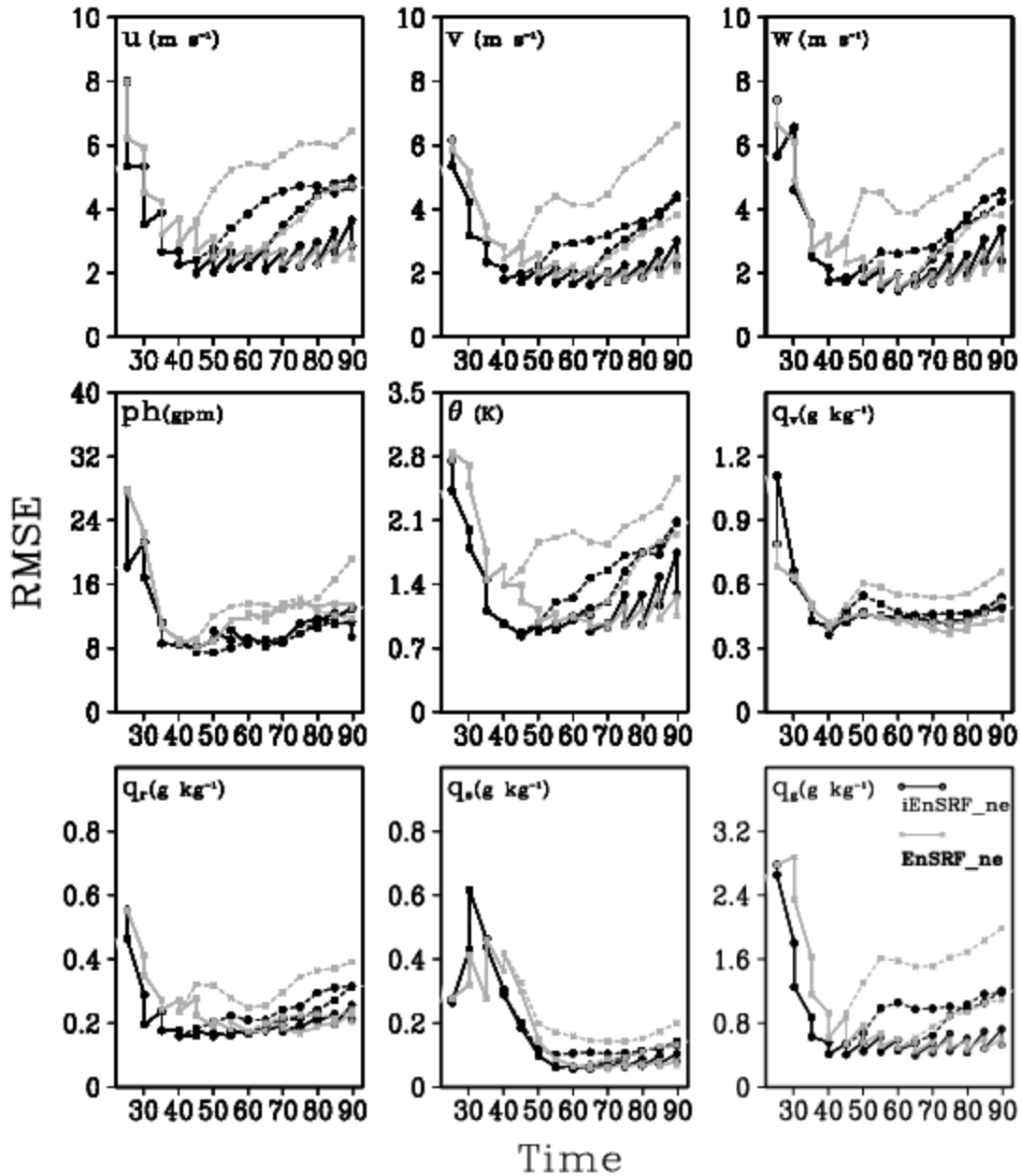


Figure 4. The evolution of RMS errors for experiments EnSRF_ne (grey line) and iEnSRF_ne (black line). Solid lines represent errors within the assimilation window while dash lines stand for errors of deterministic forecasts launched from the ensemble mean analyses at 40 and 60 minutes.

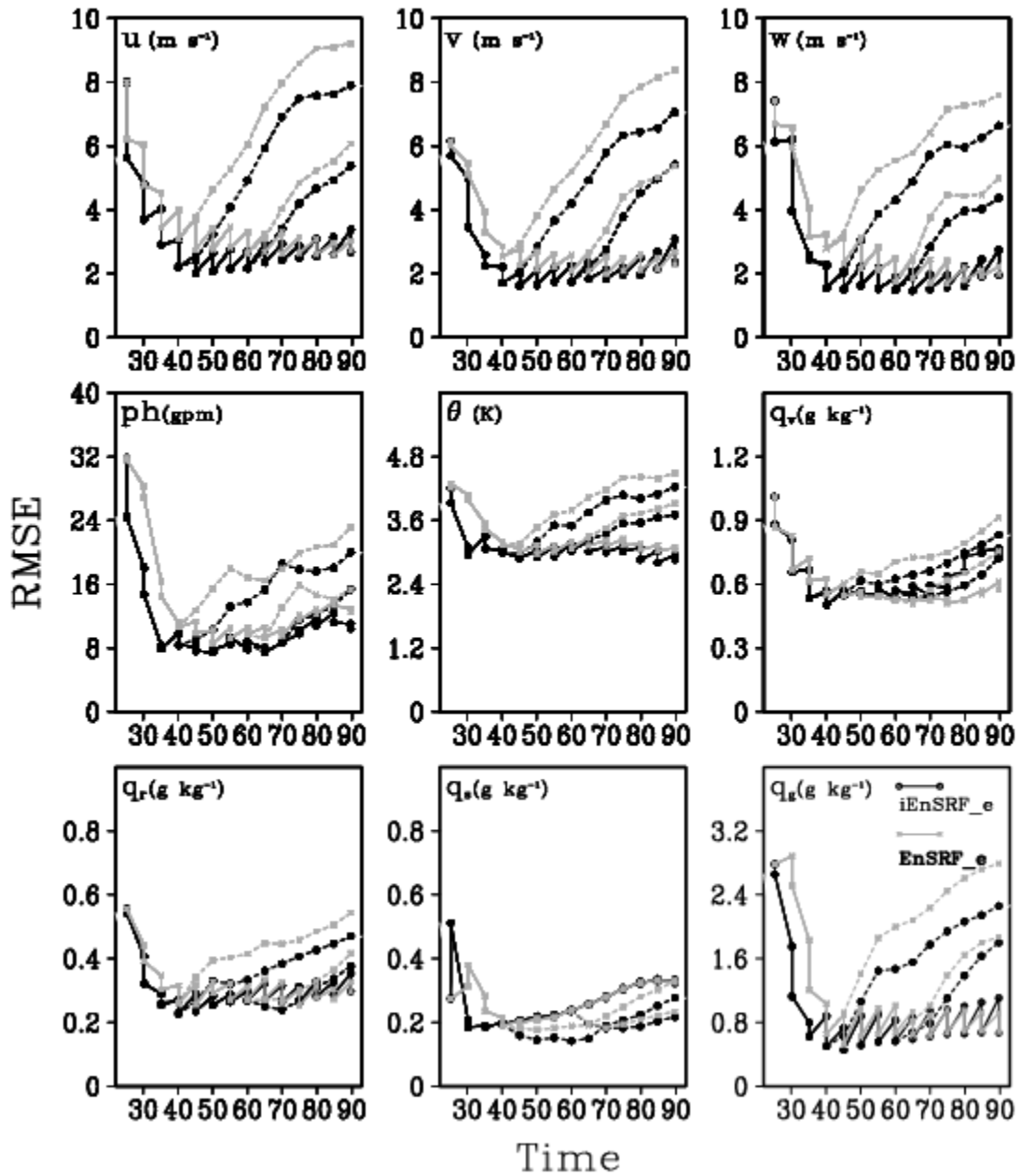


Figure 5. The same as Figure 4, but for experiments EnSRF_e (grey line) and iEnSRF_e (black line).

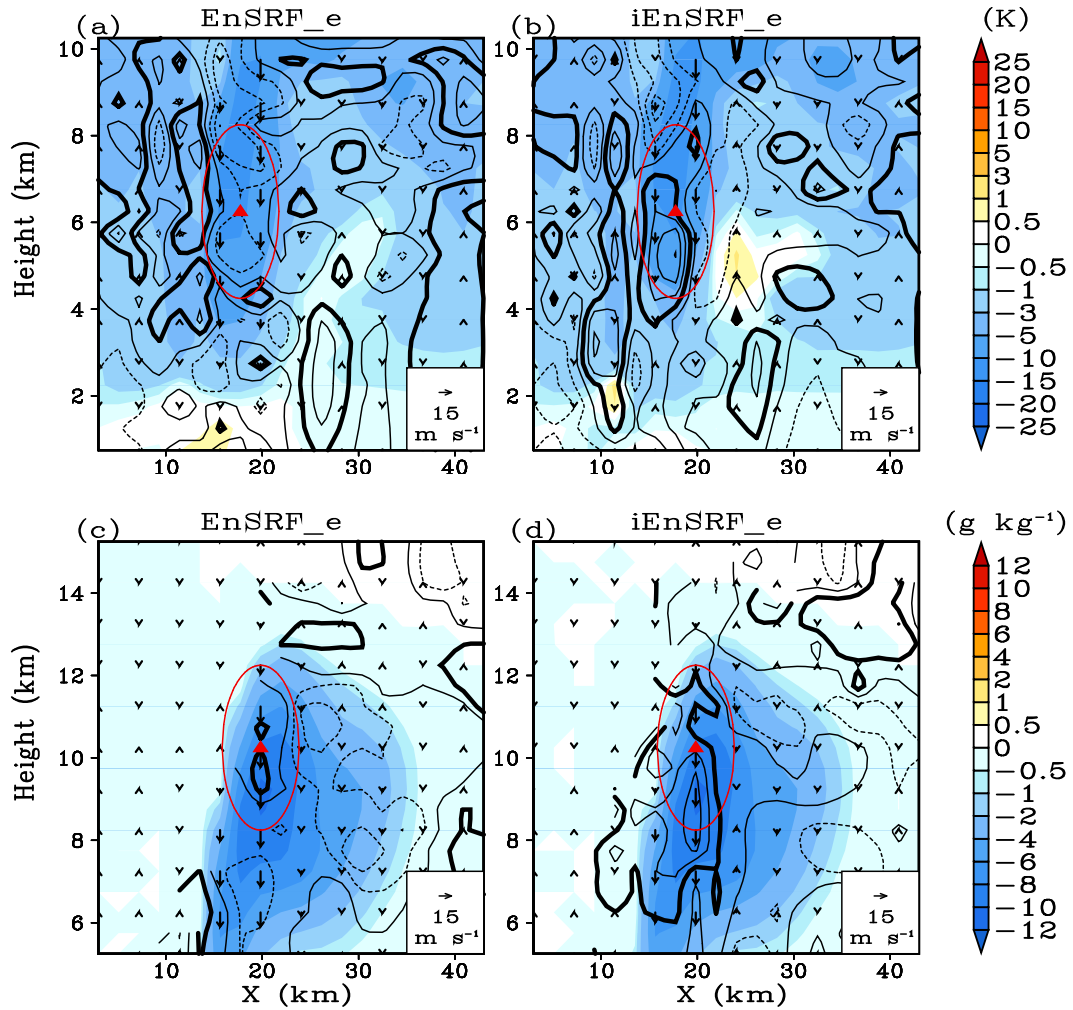


Figure 6. Vertical cross sections of forecast errors, calculated as the ensemble mean minus the truth (error field shaded with vertical velocity error shown as vertical vectors), and the correlation coefficients of forecast errors (contours at intervals of 0.2), at 25 min, the time of first analysis, in an x-y plane at $y=30$ km. The 0.2 correlation contours are in bold. The red ellipse is the 0.2 contour for the localization coefficient for the observation located at the red triangle. For iEnSRF_e the forecasts are at the end of the third iteration. The upper panels show the forecast errors of θ (shaded) and w (vertical vectors) and forecast error correlation coefficient between w at the point marked by the red triangle and θ at the grid point, for EnSRF_e (left) and iEnSRF_e (right). The lower panels are the same as the upper panels except θ is replaced by q_g .

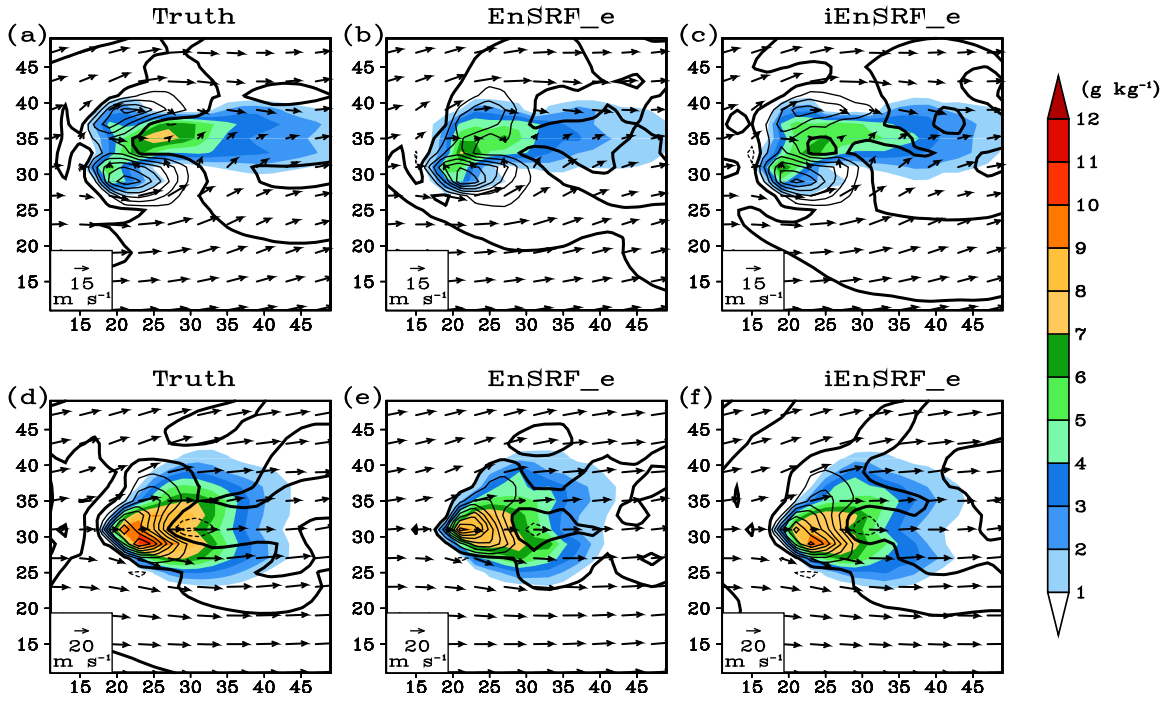


Figure 7. The graupel mix ratio (shaded), vertical velocity (contoured at intervals of 4 m s^{-1}) and horizontal wind vectors at 40 min. for the truth simulation (left), EnSRF analysis (middle) and iEnSRF_e analysis (right), at 5 km (upper panels) and 10 km (lower panels) AGL. w contours are shown in bold.

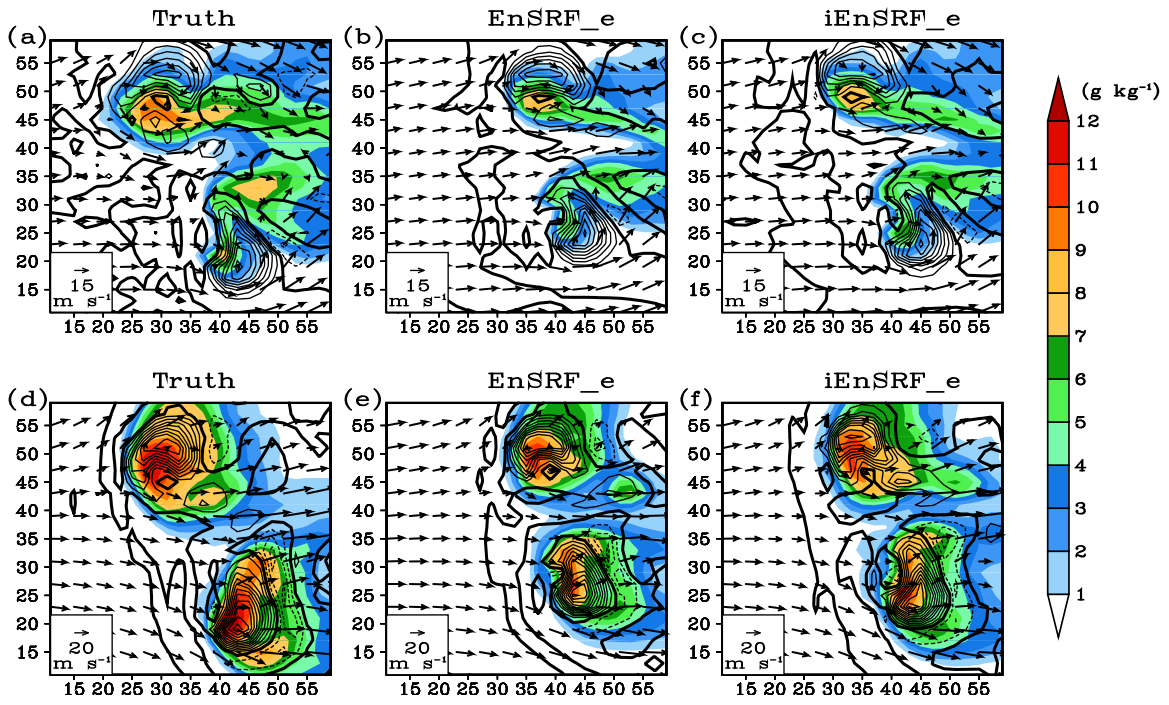


Figure 8. The same as Figure 7, but for deterministic forecasts at 90 min starting from the ensemble mean analyses at 40 min. in EnSRF_e (mid panels) and iEnSRF_e (right panels), as compared to the truth (left panels).